

Elliptic flow at RHIC and LHC in the string percolation approach

I. Bautista [†], J. Dias de Deus ^{*} and C. Pajares [†]

July 9, 2021

Abstract

The percolation of strings gives a good description of the RHIC experimental data on the elliptic flow, v_2 and predicted a rise on the integrated v_2 of the order of 25% at LHC such as it has been experimentally obtained. We show that the dependence of v_2 on p_T for RHIC and LHC energies is approximately the same as it has been observed, for all the centralities. We show the results for different particles and the dependence of v_2 on the centralities and rapidity. Our results are compatible with a small value of the ratio η/s in the whole energy range such as it was expected in the percolation framework.

1 Introduction

A major breakthrough was the discovery at RHIC experiments of a large elliptic flow v_2 [1-9]. The observed anisotropic flow can be understood only if the particles measured in the final state depend not only on the physical conditions realized locally at their production point but also on the global geometry of the event. In a relativistic local theory, this non-local information can only emerge as a collective effect, requiring interactions between the relevant degrees of freedom, localized at different points of the collision region. This anisotropic flow is particularly unambiguous and convincing

^{*}CENTRA, Departamento de Física, IST, Av. Rovisco Pais, 1049-001 Lisboa, Portugal

[†]IGFAE and Departamento de Física de Partículas, Univ. of Santiago de Compostela, 15782, Santiago de Compostela, Spain

manifestation of collective dynamics [10]. The large elliptic flow v_2 can be qualitatively explained as follows. In a collision at high energy the spectator nucleons are fast enough to move away leaving behind at mid-rapidity and almond shaped azimuthally asymmetric overlap region filled with the QCD matter. This spatial asymmetry implies unequal pressure gradients in the transverse plane, with a larger density gradient perpendicular to the reaction plane (in-plane). As a consequence of the subsequent multiple interactions between the degrees of freedom involved, the spatial asymmetry leads to anisotropy in the momentum space [4,11,12]. The final particle transverse momentum is more likely to be in-plane than in the out-plane, with $v_2 > 0$ as predicted [5].

The general idea has been realized in various mechanisms for the source of elliptic flow. A convenient and successful way to describe the flow anisotropy is achieved in the hydrodynamical approach [6,8], taking into account the asymmetric shape of the nuclei overlap in the transverse plane at values of the impact parameter b different from zero. The description of course assumes collective effects to be responsible of the flow. The microscopic framework of the hydrodynamics approach, as well as the understanding of the required early thermalization remain open questions. The percolation of strings [13,14] can provide the microscopic picture and the answer of these questions.

In a heavy ion collision at high energy, strings stretched between the partons of the projectile and the target are formed. Each string in the transverse space looks like disk of area πr_0^2 , with $r_0 \simeq 0.2 - 0.3$ fm due to the confinement. As the energy and/or the size of colliding objects grows the number of strings increases and the strings overlap forming clusters, whose behavior is determined by the color field inside which is given by the vectorial sum of the color field of the individual string. In this way, the formation of clusters can be seen as interactions of the partons of the individual strings with the corresponding color rearrangement. On the other hand, a local temperature can be defined associated to the fragmentation of the string via the Schwinger mechanism [15,16], and in the same way a temperature can be associated to the cluster formed from many individual strings. As far as this cluster covers most of the total interaction area, (what happens if the string density is over the critical percolation threshold) this temperature becomes a global temperature determined by the string density. This fact, together with the good description of the elliptic flow of RHIC data makes the percolation of strings a good candidate to be the initial state for hydrodynamical description.

The elliptic flow was studied in the framework of percolation in references [17-20] leading to the developments of analytical formulae for v_2 including the dependence on transverse momentum, which were successfully compared with the RHIC experimental data [17-18]. In reference [20] were given arguments in favor of the methods used previously.

In this paper we present our results for LHC energies. Previously, we already anticipated a rise of around 25% [19] for the integrated elliptic flow as it has been obtained experimentally [21]. In the evaluation, the main source of uncertainties is the string density due to the uncertainties in the number of strings and its dependence on the energy and centrality. To avoid these uncertainties we determine the string density in $Pb - Pb$ at LHC at different centralities comparing the corresponding formula in percolation with the data of the ALICE collaboration [22]. Given the string density, the elliptic flow is obtained using our analytical formula.

We find that v_2 for $p_T < 0.8$ GeV/c is very similar at LHC and RHIC energies, being slightly larger for $p_T > 0.8$ GeV/c. Concerning the rapidity distribution there is no longer a triangle shape and a flatten distribution is obtained for $|y| < 4$. Also there is not limiting fragmentation in the same way that in percolation there is not limiting fragmentation in $\frac{dN}{dy}$. We obtain a very reasonable overall agreement with the experimental data, compatible with the existence of a partonic fluid with a low ratio between the shear viscosity and the entropy density in the whole energy range from RHIC to LHC. This low ratio for this energy range was expected in the percolation framework [23-24].

The plan of the paper is as follows. In the next section we present a brief introduction to percolation of strings. In section 3 we describe the obtention of the analytical formulas for the elliptic flow. In section 4 we discuss our results comparing with LHC and RHIC experimental data. Finally, in section 5 we present our conclusions.

2 The string percolation model

In the collision of two nuclei at high energy, the multiparticle production is described in terms of color string stretched between the partons of the projectile and the target. These strings decay into new ones by $q\bar{q}$ or $qq - \bar{q}\bar{q}$ pair production and subsequently hadronize to produce hadrons. Due to the confinement, the color of these strings is confined to a small area in

transverse space $S_1 = \pi r_0^2$ with $r_0 \simeq 0.2 - 0.3\text{fm}$. This value corresponds to the correlation length of the QCD vacuum [25]. With increasing energy and/or atomic number of the colliding particles, the number of strings grows and they start to overlap forming clusters. At a certain critical density, a macroscopical cluster appears, which marks the percolation phase transition. This value corresponds to the value $\rho_c = 1.18 - 1.5$ (depending on the type of the profile functions of the nucleus employed, homogeneous or Wood-Saxon) where the variable $\rho = N_s S_1 / S_A$, and S_A

$$S_A = 2R_A^2 [\cos^{-1}(\beta) - \beta \sqrt{1 - \beta^2}] \quad (1)$$

with

$$\beta = \frac{b}{2R_A} \quad (2)$$

is the overlapping area of the nucleus. In order to describe the behavior of the clusters formed by several overlapping strings we must introduce some dynamics. We assume that a cluster of n strings behaves as a single string with an energy-momentum that corresponds to the sum of the energy-momentum of the individual strings with a higher color field, corresponding to the vectorial sum of the color field of each individual string. In this way [14][26] we can compute the mean multiplicity μ_n and the mean transverse momentum squared $\langle p_T^2 \rangle_n$ of the particles produced by a cluster:

$$\mu_n = \sqrt{\frac{nS_n}{S_1}} \mu_1, \text{ and } \langle p_T^2 \rangle_n = \sqrt{\frac{nS_1}{S_n}} \langle p_{T1}^2 \rangle \quad (3)$$

where μ_1 and $\langle p_T^2 \rangle_1$ are the mean multiplicity and mean p_T^2 of particles produced by a single string and S_n is the total area occupied by the n disks, which can be different for a different configurations even if the clusters have the same number of strings. Note that if the strings just touch each other, $S_n = nS_1$, and the strings act independently of each other. In contrast, if they fully overlap $S_n = S_1$, and it is obtained the largest suppression of the multiplicity and the largest increase of the transverse momentum. In the limit of high density, one obtains [14][26]

$$\langle n \frac{S_1}{S_n} \rangle = \frac{\rho}{1 - e^{-\rho}} \equiv \frac{1}{F(\rho)^2} \quad (4)$$

and equations (3) transforms into analytical ones

$$\mu = N_s F(\rho) \mu_1, \quad \langle p_T^2 \rangle_1 = \frac{\langle p_T^2 \rangle_1}{F(\rho)} \quad (5)$$

In the mid-rapidity region, the number of strings is proportional to the number of collisions $N_{coll} \sim N_A^{4/3}$ and grows like $s^{2\Delta}$. Therefore $\rho \sim N_A^{2/3}$, and $\mu \sim N_A$ and $\mu \sim s^\Delta$. In other words, the multiplicity per participant is almost independent of N_A (the only dependence on N_A arises from the factor $\sqrt{1 - e^{-\rho}}$ in eq. (5)). Outside the midrapidity, N_s is proportional to N_A instead of $N_A^{4/3}$. Therefore, there is an additional suppression factor $N_A^{1/3}$ compared to central rapidity.

Concerning the transverse momentum distribution, one needs the distribution $g(x, p_T)$ for each cluster and the mean squared transverse momentum of the clusters, $W(x)$. For $g(x, p_T)$ we assume the Schwinger formula $g(x, p_T^2) = \exp(-p_T^2 x)$. For the weight function, we assume the gamma distribution

$$W(x) = \frac{\gamma(\gamma x)^{k-1}}{\gamma \Gamma(k)} e^{-\gamma x} \quad (6)$$

which is the simplest distribution among the distributions stable under the size transformations [27,28]. In (6) γ and k are

$$\frac{1}{k} = \frac{\langle x^2 \rangle - \langle x \rangle^2}{\langle x \rangle^2}, \quad \gamma = \frac{k}{\langle x \rangle} \quad (7)$$

$\frac{1}{k}$ is proportional to the width of the distribution, depending on the string density ρ . At small density, there is not overlapping of strings and all the strings produce particles with the same mean transverse momentum. The width is zero and $k \rightarrow \infty$. When ρ increases there is some overlapping of strings, different clusters are formed and k decreases. The minimum of k will be reached when there are more different clusters. Above this point, the different clusters start to join and k increases. In the limit $\rho \rightarrow \infty$, there is only one cluster formed by all the produced strings and $k \rightarrow \infty$. Therefore the transverse momentum distribution $f(p_T, y)$ of the particle i is given by [28]

$$\begin{aligned} f(p_t, y) &= \frac{dN}{dp_T^2 dy} = \int_0^\infty d(x) W(x) g(p_T, x) \\ &= \frac{dN}{dy} \frac{k-1}{k} \frac{1}{\langle p_T^2 \rangle_i} F(\rho) (1 + F(\rho) p_T^2 / k \langle p_T^2 \rangle_i)^{-k(\rho)} \end{aligned} \quad (8)$$

where the dependence of k or ρ is determined by comparing (8) with the experimental data. The formula (8) is valid for all the energy, centralities and $p_T < 4 - 5$ GeV/c. In the case of baryons we must introduce minor

changes [29]. The equation (8) is the main ingredient for the evaluation of the elliptic flow.

3 Elliptic flow

The cluster formed by the strings has generally an asymmetric form in the transverse plane and acquires dimensions comparable to the nuclear overlap. This azimuthal asymmetry is at the origin of the elliptic flow in percolation. In fact, the partons emitted at some point inside the cluster have to pass a certain length through the strong color field of the cluster before they appear outside. It is natural to assume that the energy loss by the parton is proportional to the length and therefore the transverse momentum p_T of an observed particle will depend on the path length travelled and so different for different direction of emission [19].

In this way the inclusive cross section $\frac{dN}{dp_T^2 dy d\varphi} = f(p_T^2, \rho_\varphi, y)$ can be obtained from eq (8). doing the change $\rho \rightarrow \rho_\varphi$, where

$$\rho_\varphi = \rho \left(\frac{R}{R_\varphi} \right)^2 \quad (9)$$

where R and R_φ are shown in fig 1. Notice that

$$\frac{\pi R^2}{4} = \frac{1}{2} \int_0^{\pi/2} d\varphi R_\varphi^2 \quad (10)$$

Expanding $f(p_T, \rho_\varphi, y)$ around ρ or R we have

$$f(p_T, \rho_\varphi, y) \simeq \frac{2}{\pi} f(p_T, \rho, y) \left[1 + \frac{\partial \ln f(p_T^2, \rho, y)}{\partial R^2} (R_\varphi^2 - R^2) \right] \quad (11)$$

Notice that due to (10) we have

$$\int_0^{\pi/2} f(p_T, \rho_\varphi, y) d\varphi = f(p_T, \rho, y) \quad (12)$$

and from (11), finally we obtain

$$\begin{aligned} v_2(p_T^2, y) &= \frac{2}{\pi} \int_0^{\pi/2} d\varphi \cos(2\varphi) \left[1 + \frac{\partial \ln f(p_T^2, \rho, y)}{\partial R^2} (R_\varphi^2 - R^2) \right] \\ &= \frac{2}{\pi} \int_0^{\pi/2} d\varphi \cos 2\varphi \left(\frac{R_\varphi}{R} \right)^2 \left(\frac{e^{-\rho} - F(\rho)^2}{2F(\rho)^2} \right) \frac{F(\rho) p_T^2 / \langle p_T^2 \rangle_1}{(1 + F(\rho) p_T^2 / \langle p_T^2 \rangle_1)} \end{aligned} \quad (13)$$

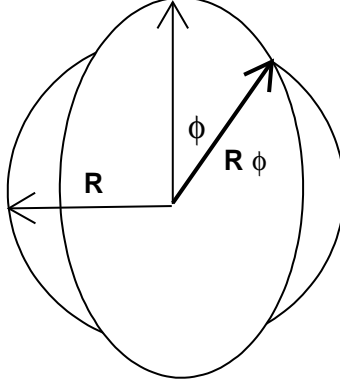


Figure 1: Azimuthal dependence of R.

having present that

$$\frac{R_\varphi}{R_A} = \frac{\sin(\varphi - \alpha)}{\sin\varphi} \quad (14)$$

$$\alpha = \sin^{-1}(\beta \sin\varphi) \quad (15)$$

for fixed \sqrt{s} and ρ , in the limit cases of $b \rightarrow 0$ and $b \rightarrow 2R_A$ we have:

(i) $b \rightarrow 0$ (i.e $\beta \rightarrow 0$ or $N_A \rightarrow A$) which implies $\alpha \rightarrow 0$, and $v_2(p_T^2, y) \rightarrow 0$.

(ii) $b \rightarrow 2R_A$ (i.e $\beta \rightarrow 1$ or $N_A \rightarrow 0$) which implies $\alpha = \varphi$ and $v_2(p_T^2, y) \rightarrow 0$ if we look now to p_T^2 dependence of v_2 , we see that $v_2 \rightarrow 0$ as $p_T^2 \rightarrow 0$ and $v_2 \rightarrow \text{constant}$ as $p_T^2 \rightarrow \infty$.

We observe that at low p_T , say $p_T < 1$, the dependence on ρ of (13) is given by $(e^{-\rho} - F(\rho)^2)/2F(\rho)$ which remain approximately constant between $\rho = 2$ and 5 which corresponds to central $Pb - Pb$ collisions at RHIC and LHC energies, therefore we expect the same v_2 at low p_T at RHIC and LHC energies.

We perform next the integration in p_T^2 , weighted by $\frac{dN}{dp_T^2 dy} / \frac{dN}{dy}$ to obtain

$$v_2 = \frac{2}{\pi} \int_0^{\pi/2} d\varphi \cos(2\varphi) \left(\frac{R_\varphi}{R} \right) \left(\frac{e^{-\rho} - F(\rho)^2}{2F(\rho)^3} \right) \frac{R}{R-1} \quad (16)$$

Again, we have $v_2 \rightarrow 0$ as $N_A \rightarrow A$ and also $v_2 \rightarrow 0$ as $N_A \rightarrow 0$. As the

bracket in (16) is in modulus a growing function of ρ , v_2 at fixed rapidity is a growing function of energy and N_A

In order to obtain formula (13) we have retained only the first term of the expansion on R^2 . This is a reasonable approximation at low p_T . For higher p_T we expect corrections of the order of 10 – 15%.

4 Results and discussion

The first formula in (5) can be written as

$$\sqrt{(1 - \exp(-\rho))\rho} = \frac{\pi r_0^2}{\mu_1} \frac{1}{S_A} \frac{dn}{d\eta} \quad (17)$$

As we know $r_0 = .2$ fm and $\mu_1 = .8$ obtained previously by comparing eq. (17) with pp data, we can compute the values of ρ from eq. (17). This allows us to eliminate the main source of uncertainties which comes from the value of the number of strings N_s and its dependence on the energy and on the centrality. We know that $N_s \sim s^{2\Delta}$ and $N_s \sim N_A^{4/3}$ and we obtained $2\Delta \simeq 2/7$ from energy-momentum conservation arguments [34], but in this paper, we determine the string density directly from the experimental data on $\frac{dN}{d\eta}$ to eliminate any uncertainty. From the centrality dependence of the experimental data [22] at $\sqrt{s} = 2.76$ TeV for $Pb - Pb$ collisions and at $\sqrt{s} = 200$ GeV for $Au - Au$ collisions we obtained the dependence of ρ on the centralities at these two energies as it is shown in Fig. (2). In Fig. (3) we show the obtained centrality dependence of $\frac{2}{N_A} \frac{dN}{d\eta}$ with the ρ -values together with the experimental data [22].

From the eq (13), we compute the transverse momentum dependence of v_2 at different centralities. The results of v_2 at different centralities are shown in figures (4) to (7), for $Pb - Pb$ at $\sqrt{s} = 2.76$ TeV compared to the RHIC results for $Au - Au$ with ALICE and STAR data [30]. We obtain at all centralities similar values of v_2 for $p_T < .8$ GeV/c and for p_T larger the LHC values are slightly larger (10%) than RHIC values. The difference is of the same size than the experimental ones. Very similar results were obtained in the percolation framework [20] using different approximations. In this case, the values found are the same at RHIC and LHC in the whole p_T range.

At $\sqrt{s} = 5.5$ TeV, from the formula (13) we expect that v_2 for low p_T would be slightly smaller than at $\sqrt{s} = 2.76$ and almost equal at higher p_T .

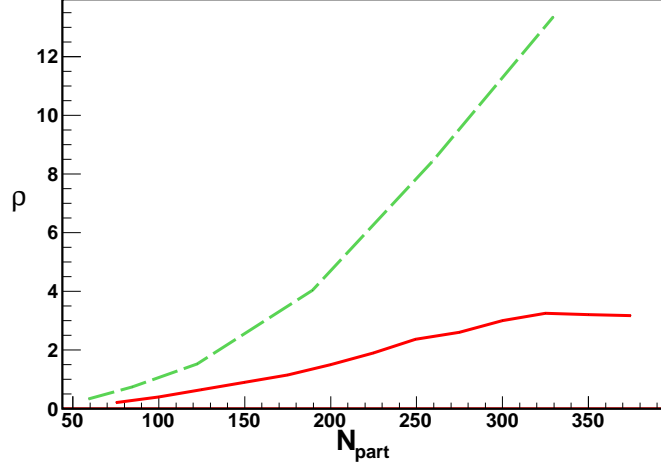


Figure 2: String density dependence with the number of participants, dashed and solid lines correspond to $\sqrt{s} = 2.76$ TeV and $\sqrt{s} = 200$ GeV energies respectively.

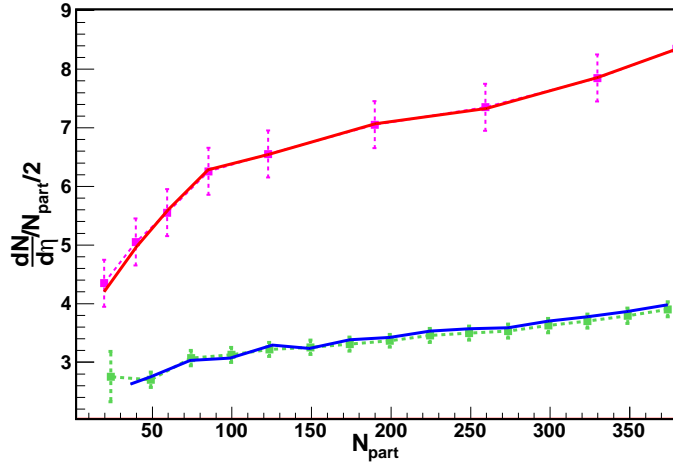


Figure 3: lines in red and blue correspond to the dependence for the $\sqrt{s} = 2.76$ TeV and $\sqrt{s} = 200$ GeV energies, errorbars in green and pink correspond to ALICE data [22] and PHENIX data [31] respectively.

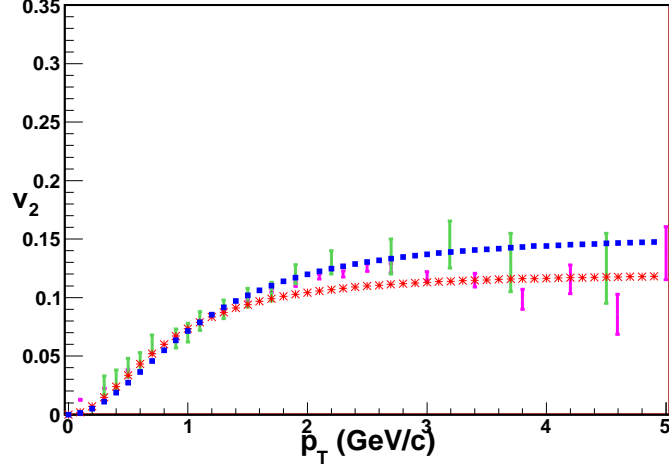


Figure 4: Stars in red and blue squares correspond to our predictions for $\sqrt{s} = 200$ GeV and $\sqrt{s} = 2.76$ TeV energies, and errorbars in green and pink are the respective data from references [22] [30] for centrality 10 – 20%.

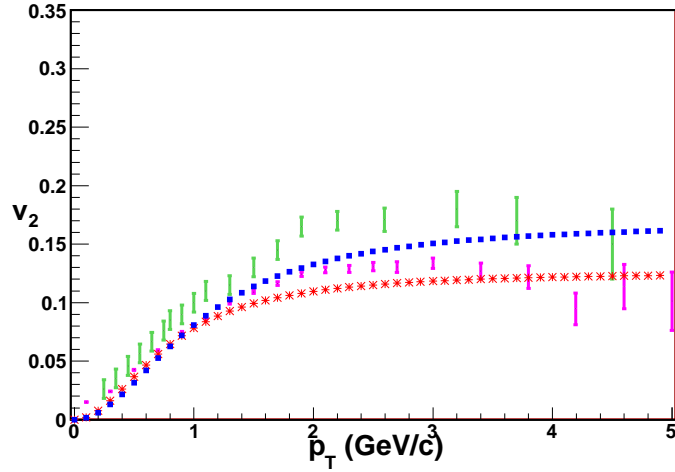


Figure 5: Stars in red and blue squares correspond to our predictions for $\sqrt{s} = 200$ GeV and $\sqrt{s} = 2.76$ TeV energies, and errorbars in green and pink are the respective data from references [22] [30] for centrality 20 – 30%.

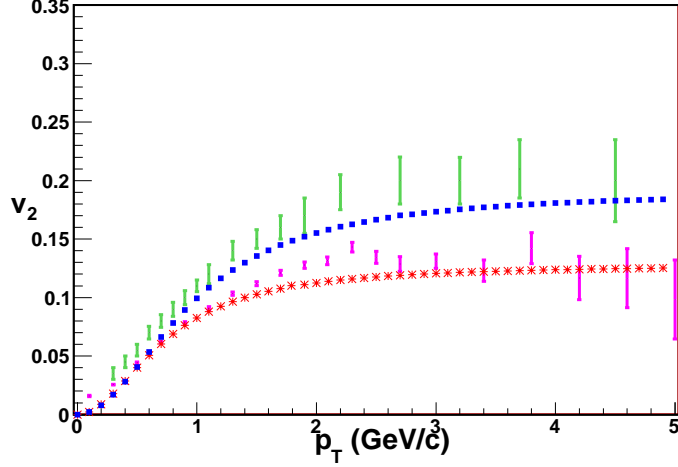


Figure 6: Stars in red and blue squares correspond to our predictions for $\sqrt{s} = 200$ GeV and $\sqrt{s} = 2.76$ TeV energies, and errorbars in green and pink are the respective data from references [22] [30] for centrality 30 – 40%.

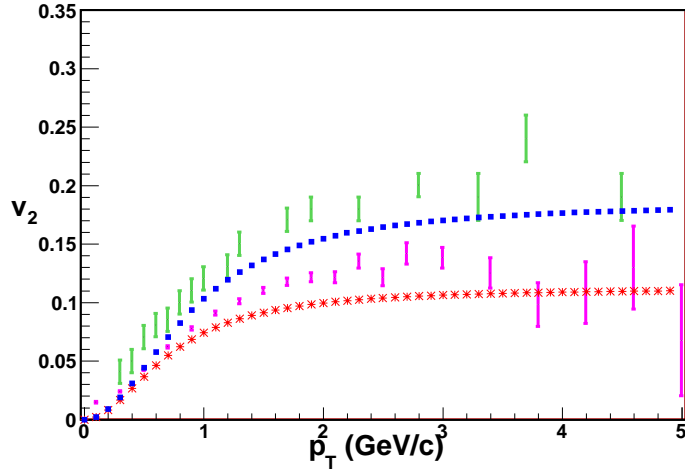


Figure 7: Stars in red and blue squares correspond to our predictions for $\sqrt{s} = 200$ GeV and $\sqrt{s} = 2.76$ TeV energies, and errorbars in green and pink are the respective data from references [22] [30] for centrality 40 – 50%.

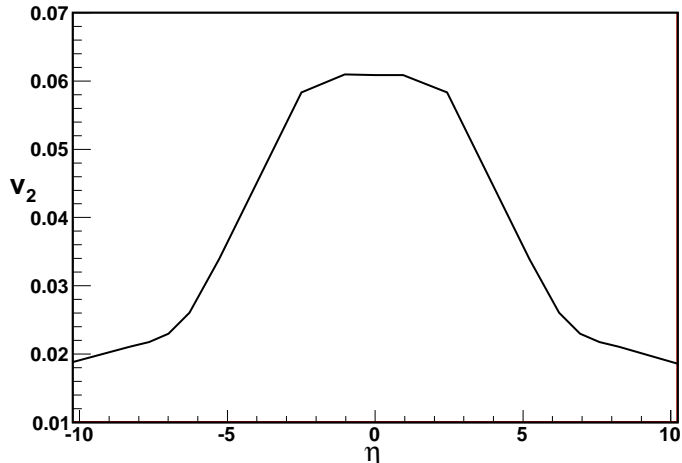


Figure 8: Results for elliptic flow dependence with pseudorapidity in $Pb-Pb$ collisions at $\sqrt{s} = 2.76$ TeV with $N_{part} = 211$.

In Fig. (8) and (9) we plot the rapidity dependence of v_2 for central $Pb-Pb$ collisions at $\sqrt{s} = 2.76$ TeV and for $Au-Au$ collisions at $\sqrt{s} = 200$ GeV at $N_{part} = 211$ respectively, obtained from eq(16). In Fig. (9), we include the corresponding experimental data [32]. The integrated v_2 obtained is around 25% higher at LHC than at RHIC energies in agreement with the experimental data [21]. We observe a breaking of limiting fragmentation as it is expected for percolation in $\frac{dN}{dy}$ [33].

In Fig. (10), we compare the values of v_2 at different centralities with the experimental data, obtaining a good agreement. In fig (11) we show the results at $\sqrt{s} = 2.76$ TeV for π , k , and p at a centrality of 40–50% for $Pb-Pb$ collisions. In figure (12) we check the constituent quark scaling plotting the ratio between the elliptic flow and the number of constituents as a function of the ratio between the kinetic energy and the number of constituents at $\sqrt{s} = 2.76$ TeV. In this case, we observe an approximate scaling at low values of the kinetic energy. For high values, we have deviations of the scaling at $\sqrt{s} = 2.76$ TeV of the order of 20%. In our evaluations, we have neglected terms that for $p_T > 1$ GeV/c can give contributions of the same order.

The similar values of v_2 found for LHC and RHIC energies points out the existence of a liquid of very low value of the ratio between the shear viscosity

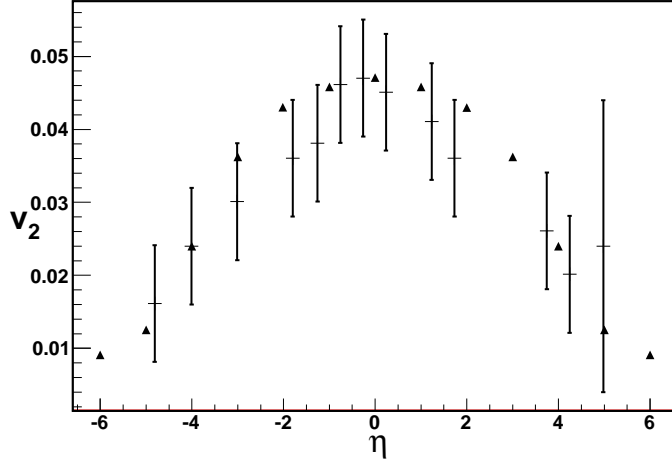


Figure 9: Triangles show the corresponding results for elliptic flow dependence with pseudorapidity in $Au - Au$ collisions at $\sqrt{s} = 200$ GeV with $N_{part} = 211$, compare to data from PHOBOS [32].

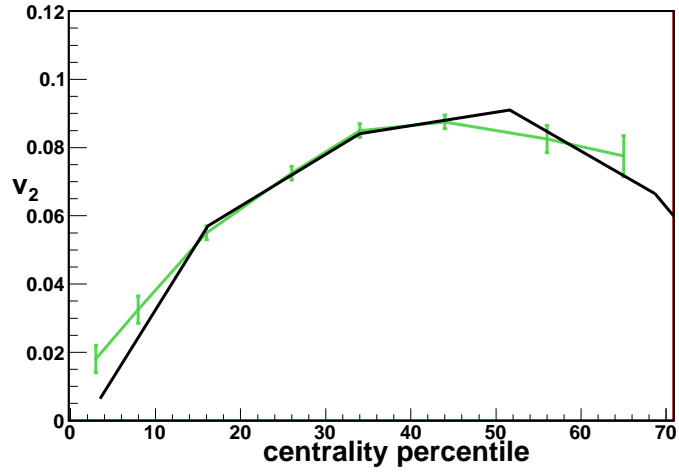


Figure 10: Integrated v_2 at $\sqrt{s} = 2.76$ TeV compared with ALICE data[22].

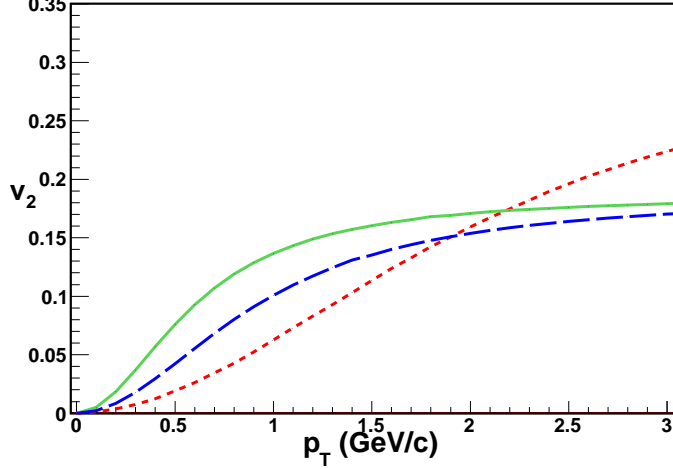


Figure 11: Red dotted line, green solid line and blue dashed line are correspond to the proton, kaon, and pion predictions for central $Pb - Pb$ collisions at $\sqrt{s} = 2.76$ TeV.

η and the entropy, s . This low ratio is expected in percolation approach [23]. In fact, the ratio is given by

$$\frac{\eta}{s} \simeq \frac{T}{5n\sigma_{tr}} \quad (18)$$

where T is the temperature, n the number of effective sources per unit volume and σ_{tr} is the transport cross section, According to the second part of the formula (5), the transverse correlation length is $r_0\sqrt{F(\rho)}$ and therefore

$$\sigma_{tr} = \pi r_0^2 F(\rho) = S_1 F(\rho) \quad (19)$$

On the other hand, the number of sources is given by the ratio between the area covered by strings and the area corresponding to the transverse correlation length

$$N = \frac{(1 - e^{-\rho})S_A}{F(\rho)S_1} \quad (20)$$

and therefore

$$n = \frac{(1 - e^{-\rho})}{F(\rho)S_1 L} \quad (21)$$

with $L \simeq 1$ fm.

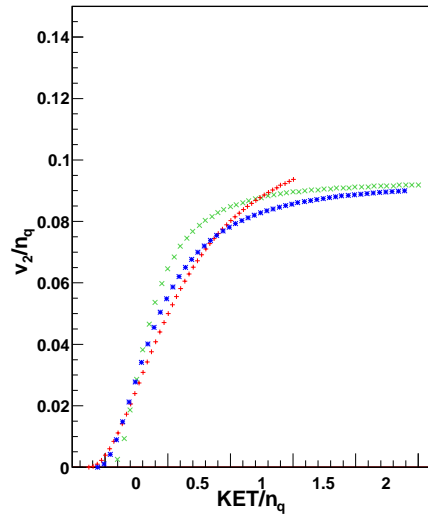


Figure 12: Elliptic flow scaling with the number of quark constituents for central $Pb - Pb$ collisions at $\sqrt{s} = 2.76$ TeV. Symbols (+) in red, (*) in blue and (x) in green are used for protons, kaons and pions respectively.

Finally, we can relate the temperature to the tension of the cluster [16] resulting

$$T = (\langle p_T^2 \rangle_1 / 2F(\rho))^{1/2} \quad (22)$$

Introducing (19), (20), (21) and (22) into (18) we obtain

$$\frac{\eta}{s} = \frac{\langle p_T \rangle_1 L}{5\sqrt{2}} \frac{\rho^{1/4}}{(1 - e^{-\rho})^{5/4}} \quad (23)$$

where we have approximated $(\langle p_T^2 \rangle_1)^{1/2} \simeq \langle p_T \rangle_1$. For $\langle p_T \rangle_1 = 200$ MeV/c, close to the threshold of percolation $\rho \simeq 1.2 - 1.5$, we obtain $\eta/s \simeq 0.2$ and for $\rho \simeq 3 - 5$ we obtain $\eta/s \simeq .25$. The ratio grows slowly, as $\rho^{1/4}$ remaining low between RHIC and LHC energies. Let us remark, that this low ratio is due to the small transverse correlation length, decreasing as the energy increases compensating the increasing of the effective number of sources in such a way that the mean path length $\lambda = 1/n\sigma = \frac{L}{(1-e^{-\rho})}$ remains almost constant.

5 Conclusions

The close analytical formulas obtained in the percolation framework from the approximated transverse momentum distribution allow us to compute the elliptic flow once the string density is known, which is fixed from the experimental data at LHC and RHIC energy. The transverse momentum dependence of v_2 and its values are very similar at RHIC and LHC energies for all centralities, in agreement with the experimental data. The integrated elliptic flow at mid rapidity is around 25% higher at $\sqrt{s} = 2.76$ TeV than at $\sqrt{s} = 200$ GeV and in the rapidity dependence of the elliptic flow there is no longer a triangle shape shown at RHIC. In the percolation framework there is not limiting fragmentation for both v_2 and dN/dy . The whole picture is consistent with the formation of a fluid with a low ratio between shear viscosity and entropy in the range of energies of RHIC and LHC such as it is expected in percolation. The percolation framework provide us with a microscopic partonic picture which explains the early thermalization and the large interaction required by the hydrodynamical approach.

Acknowledgments.

We thank B. K. Srivastava, M. A. Braun, N. Armesto and C. Salgado, for useful discussions.

J. D. D. thanks the support of the FCT/Portugal project PPCDT/FIS/575682004.

I. B, and C. P. were supported by the project FPA2008-01177 of MICINN, the Spanish Consolider Ingenio 2010 program CPAN and Conselleria Educacion Xunta de Galicia.

References

1. K. Adcox *et al.* [PHENIX Collaboration], Nucl. Phys. A **757** (2005) 184.
2. J. Adams *et al.* [STAR Collaboration], Nucl. Phys. A **757**, 102 (2005).
C. Adler *et al.* [STAR Collaboration], Phys. Rev. Lett. **87**, 182301 (2001).
3. S. Manly *et al.* [PHOBOS Collaboration], Nucl. Phys. A **774**, 523 (2006).
4. N. Borghini and U. A. Wiedemann, J. Phys. G **35**, 023001 (2008).
5. J. Y. Ollitrault, Phys. Rev. D **46**, 229 (1992).
6. P. Huovinen, P. F. Kolb, U. W. Heinz, P. V. Ruuskanen and S. A. Voloshin, Phys. Lett. B **503**, 58 (2001).
7. L. Bravina, K. Tywoniuk, E. Zabrodin, G. Burau, J. Bleibel, C. Fuchs and A. Faessler, Phys. Lett. B **631**, 109 (2005).
8. D. Teaney, J. Lauret and E. V. Shuryak, Phys. Rev. Lett. **86**, 4783 (2001). T. Hirano, U. W. Heinz, D. Kharzeev, R. Lacey and Y. Nara, Phys. Rev. C **77**, 044909 (2008).
9. D. Molnar and M. Gyulassy, Nucl. Phys. A **698**, 379 (2002).
10. M. Bleicher and X. Zhu, Eur. Phys. J. C **49**, 303 (2007).
11. P. F. Kolb and U. W. Heinz, arXiv:nucl-th/0305084.
12. D. A. Teaney, arXiv:0905.2433 [nucl-th].
13. N. Armesto, M. A. Braun, E. G. Ferreira and C. Pajares, Phys. Rev. Lett. **77** (1996) 3736 M. Nardi and H. Satz, Phys. Lett. B **442** (1998) 14
14. M. A. Braun and C. Pajares, Phys. Rev. Lett. **85** (2000) 4864 M. A. Braun, F. Del Moral and C. Pajares, Phys. Rev. C **65** (2002) 024907
15. D. Kharzeev and K. Tuchin, Nucl. Phys. A **753** (2005) 316 D. Kharzeev, E. Levin and K. Tuchin, Phys. Rev. C **75** (2007) 044903

16. J. Dias de Deus and C. Pajares, Phys. Lett. B **642** (2006) 455 P. Castorina, D. Kharzeev and H. Satz, Eur. Phys. J. C **52** (2007) 187 J. Dias de Deus, E. G. Ferreira, C. Pajares and R. Ugoccioni, Phys. Lett. B **581** (2004) 156
17. I. Bautista, L. Cunqueiro, J. D. de Deus and C. Pajares, J. Phys. G **37** (2010) 015103
18. I. Bautista, J. Dias de Deus and C. Pajares, Phys. Lett. B **693** (2010) 362
19. I. Bautista, J. D. de Deus and C. Pajares, arXiv:1011.1870 [hep-ph].
20. M. A. Braun and C. Pajares, arXiv:1008.0245 [hep-ph], to appear in Eur. Phys. J. C
21. A. K. Aamodt *et al.* [ALICE Collaboration], Phys. Rev. Lett. **105** (2010) 252302
22. K. Aamodt *et al.* [The ALICE Collaboration], Phys. Rev. Lett. **105** (2010) 252301
23. J. D. de Deus, A. S. Hirsch, C. Pajares, R. P. Scharenberg, B. K. Srivastava, (in preparation). R. P. Scharenberg, B. K. Srivastava, A. S. Hirsch Eur. Phys. J. C **71** 1510 (2011). B. K. Srivastava, arXiv 1102.0754 [nucl-ex].
24. J. D. de Deus and C. Pajares, Phys. Lett. B **695** (2011) 211
25. A. Di Giacomo, H. G. Dosch, V. I. Shevchenko and Yu. A. Simonov, Phys. Rept. **372** (2002) 319
26. M. A. Braun and C. Pajares, Eur. Phys. J. C **16** (2000) 349
27. G. Jona-Lasinio, Nuovo Cim. B **26** (1975) 99.
28. J. Dias de Deus, E. G. Ferreira, C. Pajares and R. Ugoccioni, Eur. Phys. J. C **40** (2005) 229 C. Pajares, Eur. Phys. J. C **43** (2005) 9
29. L. Cunqueiro, J. Dias de Deus, E. G. Ferreira and C. Pajares, Eur. Phys. J. C **53** (2008) 585

30. B. I. Abelev et al. (STAR Collaboration), Phys. Rev. C **77**, (2008) 054901. A. Andronic et al. (FOPI Collaboration), Phys. Lett. B **612**, 173 (2005).
31. S. S. Adler et al. (PHENIX), Phys. Rev. C **71**, 034908 (2005).
32. B. B. Back et al. [PHOBOS Collaboration], Phys. Rev. C. 72,051901 (2005) B. B. Back et al. [PHOBOS Collaboration], Phys. Rev. Lett. 97 (2006) 012301
33. P. Brogueira, J. Dias de Deus and C. Pajares, Phys. Rev. C **75** (2007) 054908
34. J. Dias de Deus, M. C. Espirito Santo, M. Pimenta and C. Pajares, Phys. Rev. Lett. **96** (2006) 162001
35. A. Adare et al. [PHENIX Collaboration] Phys. Lett. 98 **162301** (2007).